Electronic Supplementary Information (ESI)

Increased elasticity and damping capacity of diamond-like carbon coatings by immobilized C_{60} fullerene clusters

*Hee-Kyung Yang[1‡], Mahdi Khadem[12‡], Oleksiy V. Penkov[2] and Dae-Eun Kim[12]**

[1] Department of Mechanical Engineering, Yonsei University, Seoul, 03722, South Korea

[2] Center for Nano-Wear, Yonsei University, Seoul, 03722, South Korea

[‡] These authors contributed equally to the manuscript

[*] Corresponding Author; E-mail: kimde@yonsei.ac.kr

Phone: +82-02-2123-2822

This ESI contains:

ESI-1.

- The characterization of SAM with respect to the functional groups positioning using XPS.
- TEM images of C_{60}-DLC hybrid and characterization of the crystalline structure of C_{60}
- Surface energy and contact angle analysis.

ESI-2.

- Average Indentation (loading-unloading) curves of C_{60}-free DLC and C_{60}-DLC hybrid coatings.

ESI-3.

- TEM and AFM analysis of C_{60}-free DLC coating.

ESI-4.

- Nano-scratch analysis of C_{60}-free DLC and C_{60}-DLC hybrid coatings.

ESI-5.

- Wear assessment of C_{60}-free DLC coating.
- In-situ analysis (refer to the video file).

ESI-6.

- Additional details regarding FE modeling and simulation.

ESI-1. SAM and C_{60} characterization

To confirm the formation of SAMs on the Au and to determine the positioning of the cysteamine functional groups, the specimens were analyzed using XPS (K-alpha; Thermo Scientific Inc., UK) at take-off angles (TOA) of 90 and 20° (Figure S1a). The total intensity of the N1s and S2p peaks, which were used as the representatives of cysteamine functional groups (amine- and thiol-terminated, respectively), significantly decreased when the TOA decreased from 90 to 20°. Analysis of the intensities indicated a smaller corresponding decrease of the N1s peak, suggesting that the majority of sulfur atoms were positioned closer to the Au surface compared to the nitrogen atoms.[1] In other words, this analysis confirmed that the cysteamine SAMs were well positioned in which the thiol-terminated functional groups were adsorbed on the Au with amine functional groups pointing away from the surface. In addition, deconvolution of the S2p peak revealed three components (Figure S1b). The first two components were located at 162 and 163.1 eV and originated from the bonding of sulfur atoms to the Au surface.[1,2] The component centered at ~164.5 eV could be attributed to disulfide or possibly unbound sulfur.[1,3] The last component at 167.6 eV originated from oxidized sulfurs due to storage in ambient conditions prior to the XPS measurements.[4]

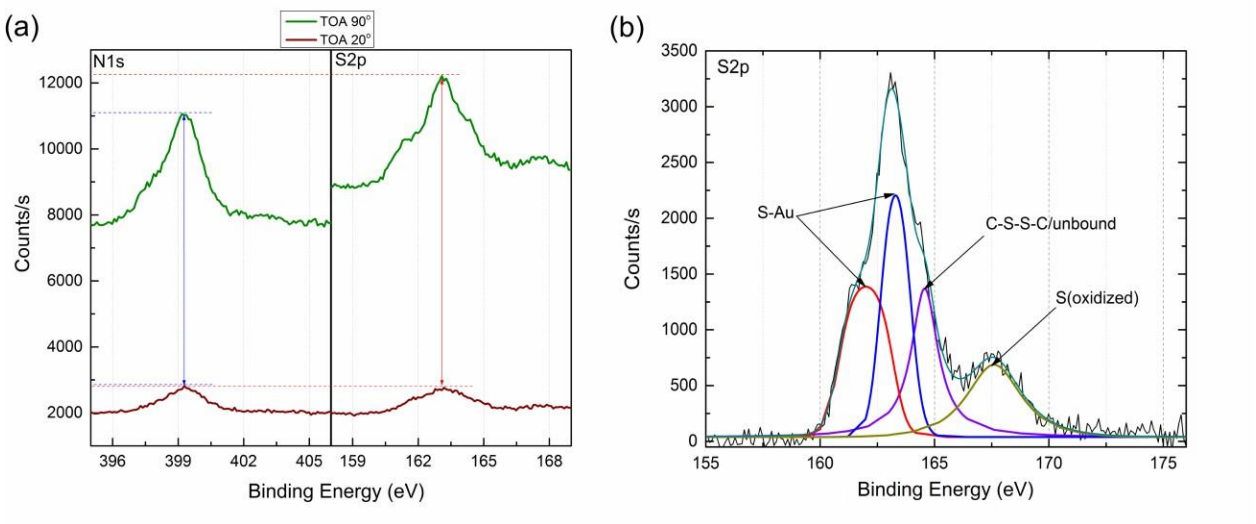

Figure S1. XPS analysis of cysteamine SAMs. (a) XPS spectra of the N1s and S2p peaks representing amine- and thiol-functional groups, respectively, taken at TOAs of 90 and 20°. (b) deconvolution of the S2p peak; components at 162 and 163.1 eV were attributed to S-Au bonding. The component at 164.5 eV originated from either disulfide or possibly unbound sulfur. The last component at 167.6 eV originated from oxidized sulfur. This analysis confirmed adsorption of thiol-functional groups to the Au surface while amine-terminated groups point away from the surface.

The presence of C_{60} fullerenes was confirmed through surface energy, atomic force microscopy (AFM; NX10, Park Systems), and high-resolution transmission electron microscopy (HR-TEM; JEM-F200, JEOL) analysis (Figure S2). To assess the surface energy, a series of contact angle measurements were performed using deionized water droplets. At least five measurements were performed to ensure reproducibility. The average contact angle was found to be 72 ± 2° which was in good agreement with reported literature values.[5,6] Multiple bright regions were observed in the cross-sectional HR-TEM images (Figure S2a circled by red dash lines). These brighter regions were believed to contain a less dense structure due to presence of voids between the C_{60} nanoparticles. The crystalline structure of

the C_{60} nanoparticles in the clusters was further analyzed as shown in Figure S2b. Accurate d-space calculations from HR-TEM data confirmed the presence of single crystalline structures (based on ICDD card no. 01-070-9118). Figures S2c and S2d provide magnified views of C_{60} clusters from random locations at the Au-DLC interface.

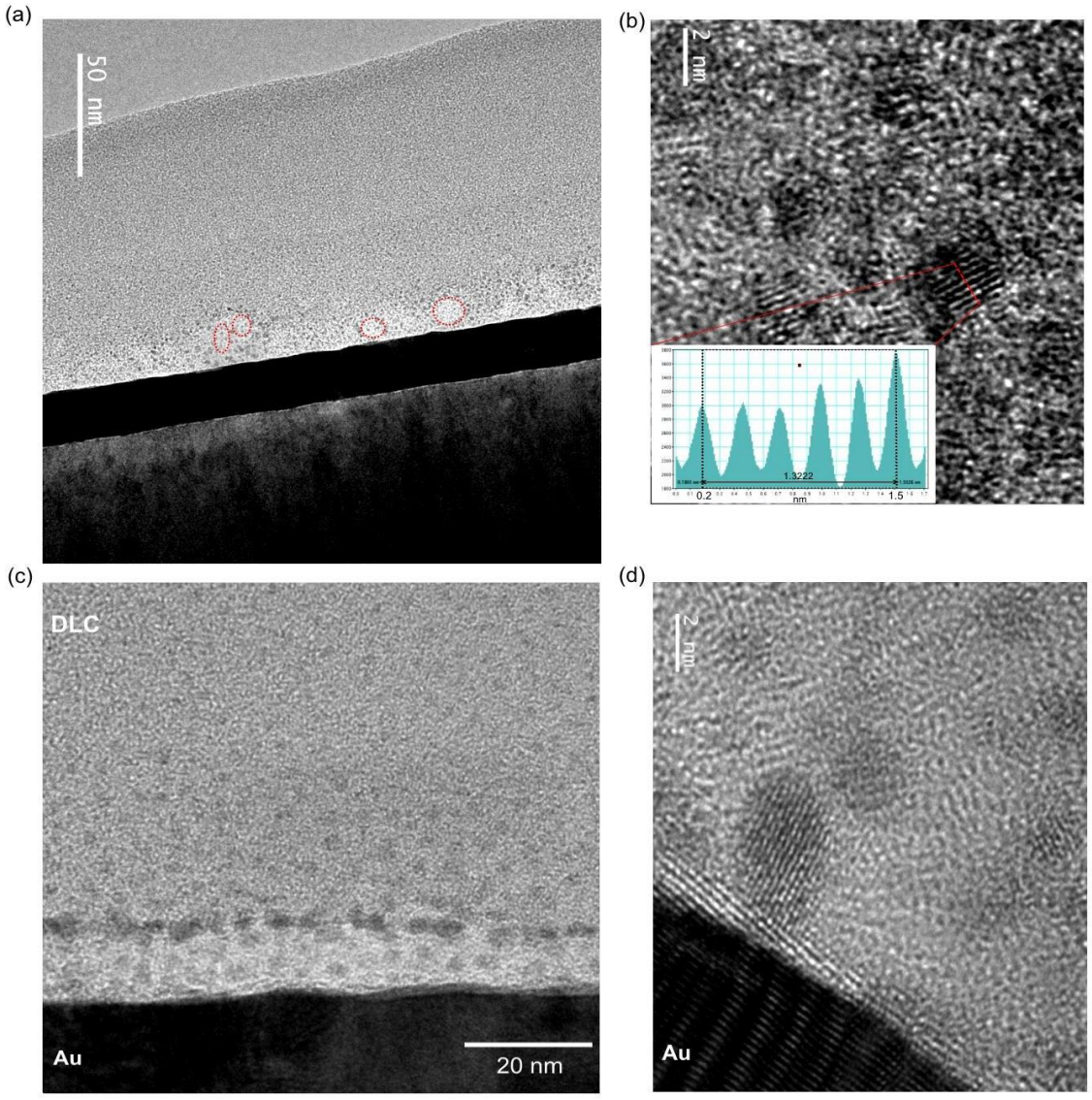

Figure S2. Cross-sectional HR-TEM analysis. (a) Overall view of a single cluster containing C_{60} nanoparticles. Regions with the brighter contrast are circled with red dash lines. (b) d-space calculation and analysis of C_{60} nanoparticles. (c,d) TEM images of C_{60} clusters taken at random locations at Au-DLC interface.

ESI-2. Average dynamic indentation (loading-unloading) curves of C_{60}-free DLC and C_{60}-DLC hybrid coatings.

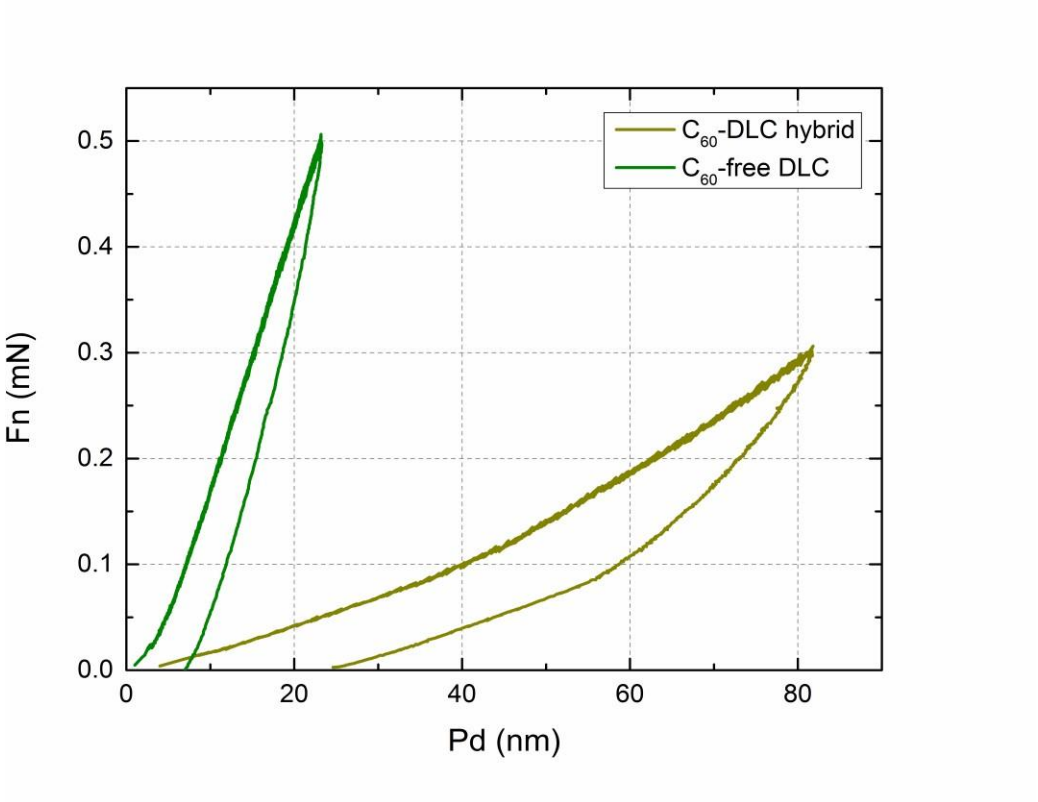

Figure S3. Evolution of dynamic indentation (loading-unloading) curves of C_{60}-free DLC and C_{60}-DLC hybrid coatings. The Oliver-Pharr method was used to characterize the elastic properties.[7]

ESI-3. TEM and AFM analyses of C_{60}-free DLC coating

The nano-structure and surface morphology of the C_{60}-free DLC coating were analyzed using AFM and TEM to compare with those of C_{60}-DLC hybrid coating (Figure S4).

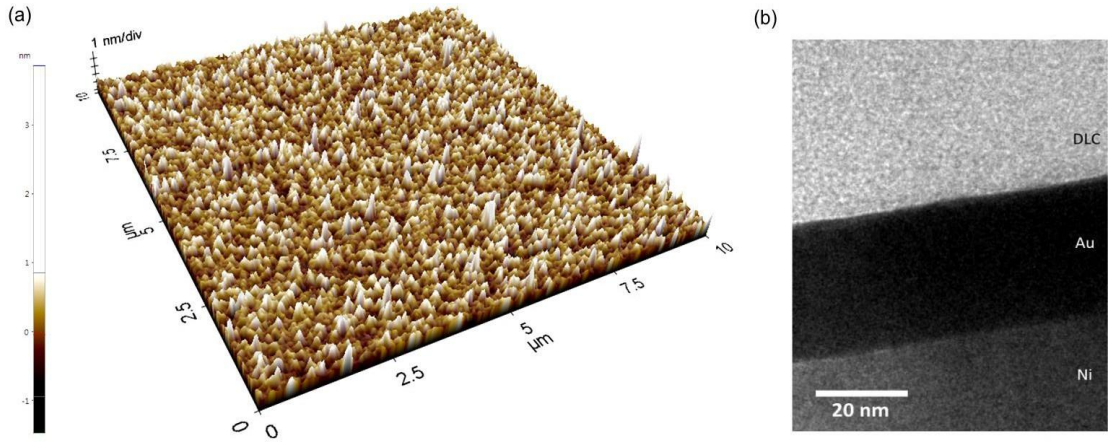

Figure S4. (a) AFM image (average surface roughness (Ra) ~1 nm) and (b) Cross-sectional HR-TEM view of the C60-free DLC coating (Ni /Au /amorphous DLC).

ESI-4. Nano-scratch analysis of C_{60}-free DLC and C_{60}-DLC hybrid coatings

Nano-scratch tests were performed using a high precision ultra nano-indenter (CSM; UNHT). The frictional force was monitored throughout the scratching process and the critical load that caused the delamination of the coating from substrate was obtained for each coating (Figure S4). As can be seen, the critical load value was found to be higher (by ~36%) in the case of C_{60}-free DLC coating (9 mN) when compared to that of C_{60}-DLC hybrid (6.6 mN). Nevertheless, as described in the main text, the C_{60}-DLC hybrid coating showed a lower wear rate than the C_{60}-free DLC coating despite the lower critical load. These results clearly indicated that the lower wear rate of C_{60}-DLC hybrid coating was not due to the higher coating adhesion, and therefore, adhesion was not the dominant parameter in determining the wear properties of the coatings.

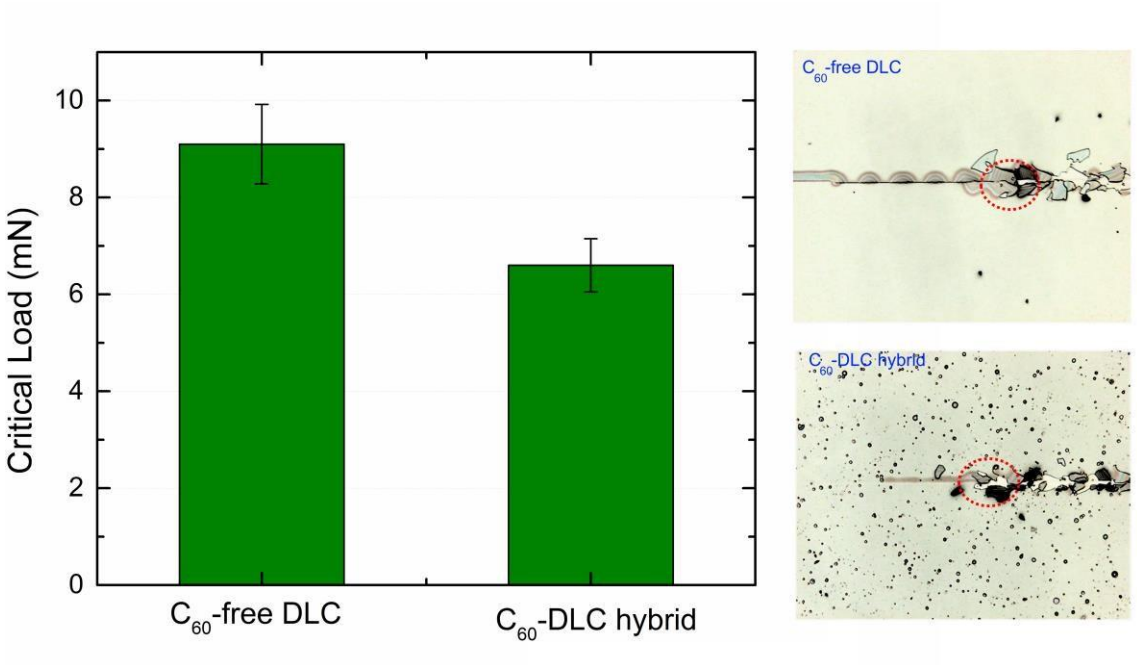

Figure S5. Nano-scratch analysis of C_{60}-free DLC and C_{60}-DLC hybrid coatings. The critical load causing the delamination (circled with the red dash line) of the coating from the substrate for the C_{60}-free DLC coating and C_{60}-DLC coating was found to be 9 and 6.6 mN, respectively.

ESI-5. Wear assessment of the C_{60}-free DLC coating

After the reciprocating contact tests, the wear tracks formed on the C_{60}-free DLC coating were analyzed using SEM (JSM6610, JEOL) equipped with EDS (OXFORD Instruments, Figure S6) for in-depth investigation of failure mechanisms. The analysis revealed the presence of two simultaneous failure mechanisms. The first mechanism that initiated DLC delamination was the accumulation of wear debris (indicated by dark blue arrows). During the reciprocating motion, the hard wear debris accelerated the crack propagation and delamination process by inducing a high stress concentration at the contact interface due to their sharp morphology. The second mechanism responsible for the severe damage of the DLC coating, originating from the brittle nature of DLC, was the formation and propagation of cracks inside the wear track (areas surrounded and indicated by the light blue dash line and arrows, respectively).

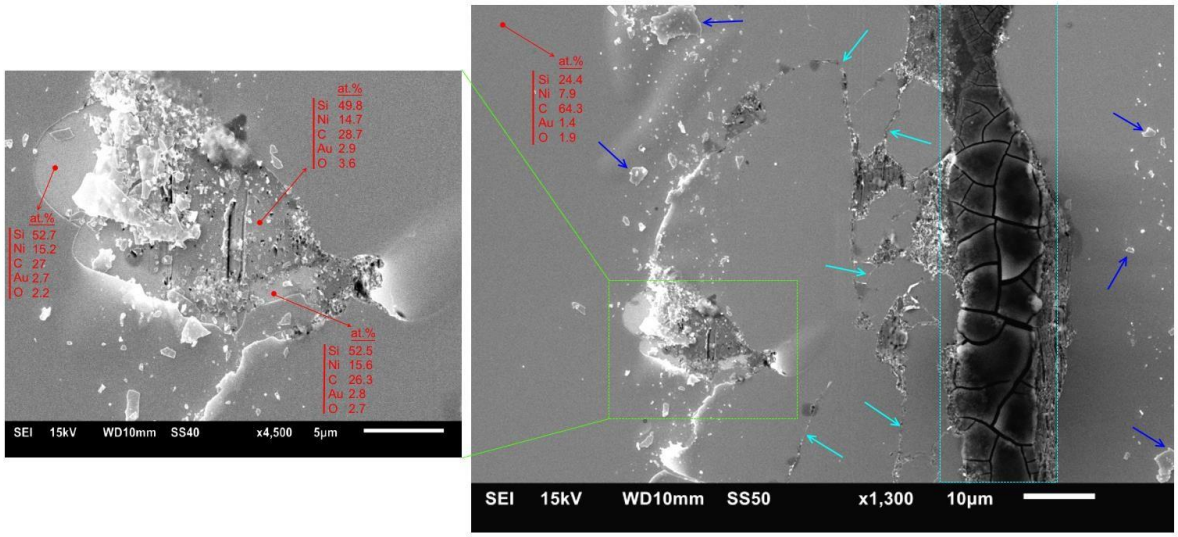

Figure S6. SEM and EDS analysis of the C_{60}-free DLC coating after reciprocating contact tests. The coating suffered from severe plastic deformation and fracture. Wear debris accumulated inside and alongside the wear track (indicated by dark blue arrows). Cracks were formed and propagated (indicated by light blue arrows and the area surrounded by dash lines). EDS elemental analysis (indicated by red dots) showed significant reduction of the carbon at.%.

In-situ monitoring of the wear track throughout the reciprocating contact sliding tests (See the video file) confirmed the failure mechanism described above. The observations revealed the formation of wear debris after approximately 200 cycles. Additional wear debris was generated as the sliding continued. Between 500 to 600 cycles the concentration of wear debris became high enough that it started affecting the coating frictional characteristics by increasing the coefficient of friction (COF signal) (Figure 4). After approximately 750 to 800 cycles, the wear debris concentration reached a critical level initiating the delamination process (the formation of a wave-like structure alongside the wear track). The cracks then

rapidly propagated inside at the contact interface resulting in coating failure at 800 to 1000 cycles.

EDS elemental analysis performed at multiple points inside the wear track (indicated by red dots) as well as outside of the wear track (as a reference point) showed significant reduction of carbon atomic percentage (at.%) inside the wear track. The carbon at.% was reduced by 60%, suggesting significant removal of the DLC coating due to contact sliding.

ESI-6. FEM Simulation

The combination of FEM and experimental analysis provided a comprehensive understanding of the mechanical behavior of the coatings. Both the C_{60}-DLC hybrid and C_{60}-free coatings were modeled for comparison and their actual structures were incorporated. For the C_{60}-DLC hybrid coating, the diameter and height of the modeled single cluster of the C_{60} molecules were 600 and 50 nm, respectively (estimated average size according to the AFM analysis). In the FEM simulation, the C_{60} cluster in the coating was assumed as a continuous phase. It should be mentioned that this simplification was allowable since the purpose of the numerical simulation was to gain insight regarding the general effect of the C_{60} layer on the elastic deformation behavior of the coating. Nevertheless, in order to match the elastic property of the actual coating, the simulations were performed using the values of Young's modulus for DLC and C_{60} layers that were directly obtained from the nano-indentation measurements. The Young's moduli of C_{60} and DLC were determined by the nano-indentation analysis of the corresponding single layer coatings.[8] The properties of the other materials were taken from the database. The simulations were performed in 2D mode to reduce the computational time.

Triangular structural meshes were generated on the C_{60}-DLC hybrid and C_{60}-free DLC coating models. Ultra-fine meshes were used at the contact region to increase the accuracy of contact analysis (Figure S7a). The mesh size increased further away from the contact region to increase the computational efficiency. The boundary of the modeled C_{60} cluster together

with the individual Ni, Au, and DLC layers are magnified and specified with green dash lines in Figures S7b and S7c.

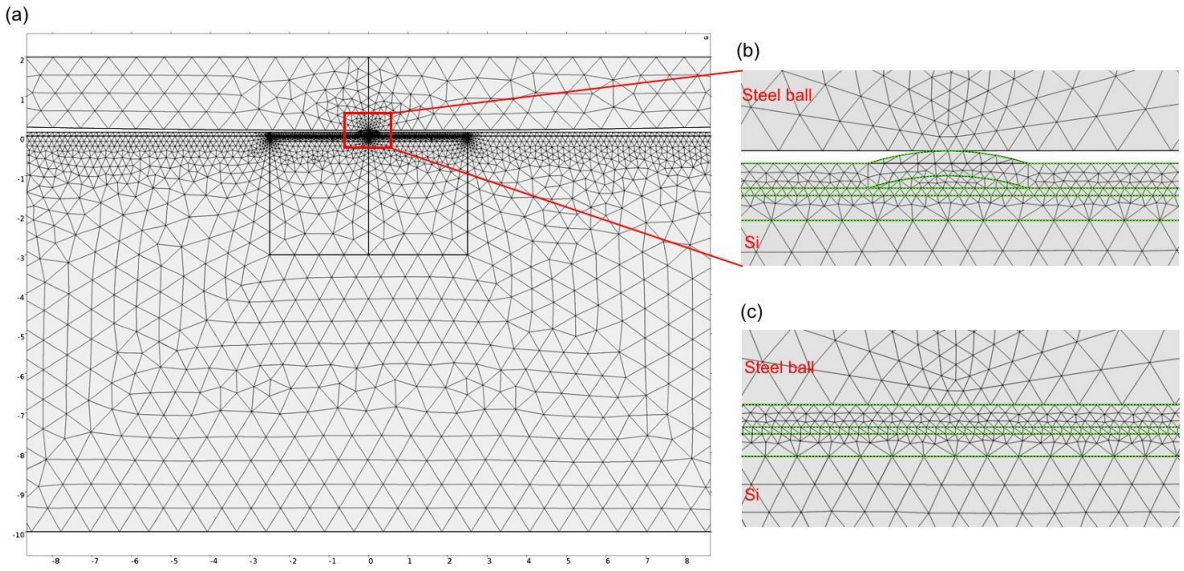

Figure S7. Constructed triangular meshes on the (a,b) C_{60}-DLC hybrid and (c) C_{60}-free DLC coating models. The contact region of coatings is magnified in (b) and (c). Green dash lines specify the boundary of the Ni, Au, DLC, and C_{60} cluster.

The following boundary conditions were imposed in the FE models: rotation and displacement were fixed at the bottom of the substrate; the ball was constrained from rotational motion. The ramped normal load (maximum: 20 mN) was normalized and calibrated to match the 2D model and to obtain the same contact stress as that I a 3D model.[9]

References

[1] M. Wirde, U. Gelius and L. Wirde, ACS. Langmuir. 1999, **15**, 6370.

[2] G. Hong, X. Tian, B. Jiang, Z. Liao, J. Wang, Y. Yang and J. Zheng, RSC. Adv., 2016, **6**, 3806.

[3] V. Spampinato, M. A. Parracino, R. Spina, F. Rossi and G. Ceccone, Front. Chem., 2016, **4**, 1.

[4] F. Wu, J. Li, Y. Tian, Y. Su, J. Wang, W. Yang, N. Li, S. Chen, S. Chen and L. Bao, Sci. Rep., 2015, **5**, 1.

[5] C. M. Kim, Korean. Chem. Soc., 2006, **27**, 2037.

[6] S. Ren, S. Yang and Y. Zhao, ACS. Lamguir., 2004, **20**, 3601.

[7] W. B. Caldwell, K. Chen, C. A. Mirkin and S. J. Babinec, ACS. Langmuir., 1993, **9**, 1945.

[8] O. V. Penkov, W. E. Pukha, A. Y. Devizenko, H. J. Kim and D. E. Kim, Nano Lett., 2014, **14**, 2536.

[9] O. V. Penkov, A. Y. Devizenko, M. Khadem, E. N. Zubarev, V. V. Kondratenko and D. E. Kim, ACS Appl. Mater. Interfaces. 2015, **7**, 18136.